Storage and release of NO_3^- and I^- via layered double hydroxides for stable lithium metal battery

Fenglin Wang,[a] Zhicheng Zheng,[a] Zuxin Wen,[a] Wenqiang Fang,[a] Chengwei Kuang,[a] Fashen Chen,[a] Hao Wan,[b] Ning Zhang,[a] Xiaohe Liu,[b,*] Renzhi Ma,[c,*] Gen Chen[a,*]

[a] School of Materials Science and Engineering, Key Laboratory of Electronic Packaging and Advanced Functional Materials of Hunan Province, Central South University, Changsha, Hunan 410083, PR China

[b] Zhongyuan Critical Metals Laboratory, School of Chemical Engineering, Zhengzhou University, Zhengzhou, Henan 450001, P. R. China.

[c] International Center for Materials Nanoarchitectonics (WPI-MANA), National Institute for Materials Science (NIMS), 1-1 Namiki, Tsukuba, Ibaraki 305-0044, Japan

* Corresponding authors: Gen Chen (geenchen@csu.edu.cn); Xiaohe Liu (liuxiaohe@zzu.edu.cn); Renzhi Ma (ma.renzhi@nims.go.jp)

Abstract

The formation of inactive lithium (Li) in lithium metal battery (LMB) is primarily attributed to the undesirable solid electrolyte interphase (SEI) components and dendritic Li deposition. Introducing $LiNO_3$ as an electrolyte additive emerges as a promising solution to these issues by in situ forming favorable nitride-rich SEI components, which effectively regulates the Li^+ stripping/plating behavior. However, the low solubility of $LiNO_3$ in carbonate electrolyte hinders the practical utilization. Herein, we propose bifunctional I^--MgAl layered double hydroxides (LDH) to dissolve $LiNO_3$ and rejuvenate inactive Li. The anion exchange capability of LDH facilitates the substitution of the native interlayered I^- with NO_3^-, leading to the formation of NO_3^--MgAl LDH. This substitution achieves the dissolution of $LiNO_3$ and serves as sustainable nitrogen source to optimize the SEI components. Additionally, the spontaneous reaction between the extracted I_3^-/I^- redox couple and inactive Li, remarkably enhancing the coulombic efficiency of Li. The special electrolyte engineering extends the lifespan of Li||$LiFePO_4$, Li||NCM and Li@Cu||$LiFePO_4$ cells. The storage and release of NO_3^- and I^- by the structural characteristics of LDH simultaneously constructs stable SEI and restores inactive Li, thereby presenting great potential for prolonging the lifespan of LMB.

Keywords: layered double hydroxides; I_3^-/I^- redox couple; $LiNO_3$; inactive Li; lithium metal battery

1. Introduction

The tremendous demands for long-range electric vehicles have driven the deep development and utilization of the next-generation high-energy-density batteries.[1, 2] Lithium (Li) metal has attracted increasing attention due to its ultrahigh specific capacity and lowest potential.[3, 4] Unfortunately, inactive Li is inevitably generated due to the continuous side reactions with electrolyte, as well as the uncontrollable growth of dendritic Li.[5, 6] Principally, the existing forms of inactive Li comprise Li^+-containing compounds of solid electrolyte interphase (SEI) and electrically isolated metallic Li debris (dead Li).[7] Specifically, dead Li is formed directly during Li stripping process, wherein partial inherent metallic Li fails to timely migrate to surface. In such a scenario, they cannot be immediately converted into Li^+ but encapsuled by SEI layer, thus losing conductive pathways with current collector.[8-10] The inactive Li is closely related to the performance degradation of LMB.[11] It is regard as the crucial reason for low coulombic efficiency (CE) of LMB and severe capacity decay during long-term cycles. Furthermore, the accumulation of inactive Li on electrode surface as well as Li dendrite growth pose major safety hazards for LMB.

Recently, strenuous efforts have been made to inhibit the generation of inactive Li by optimizing the chemical composition of electrolyte,[12-14] stabilizing interface property,[15] designing advanced structures of electrode materials,[16, 17] guiding the delithiation mechanisms of Li anode.[18] In spite of remarkable progresses achieved in dendrite-free metallic Li anodes,[19, 20] most strategies aim to reduce the generation of Li dendrites, while less studies focus on how to address the already formed Li dendrites and derived inactive Li. Reactivating dead Li further improves capacity retention and lifespan, which accounts for slowing Li consumption and enhancing interfacial stability.[21, 22] This approach lays particular emphasis on treating existing inactive Li instead of slackening off its growth rate to maintain long-term effectiveness.

The incorporation of $LiNO_3$ as an additive, without changing the fundamental composition of electrolyte, tends to uniformly deposit Li by *in situ* regulating SEI components, such as Li_3N-dominant SEI with high ionic conductivity and excellent electrochemical stability.[23-25] It is not only conducive to decrease the de-solvation energy of Li^+ solvent sheath for Li^+ migration within SEI film, but also stabilize the interface on the metallic Li surface.[26] Consequently, the improved SEI naturally averts the tree-like protrusion of Li during deposition.[27] However, the most challenging issue is the low solubility of $LiNO_3$ in carbonate electrolyte, which greatly inhibits the practical application.[28, 29] In addition, although the threat to LMB safety has significantly declined after optimizing the SEI film by introducing $LiNO_3$ in ways of transforming Li dendrites morphology from tree branch-like to lump-like, the formation of inactive Li is still inevitable. Therefore, implementing strategies for simultaneously dissolving $LiNO_3$ to optimize SEI film and recovering inactive Li are pivotal and urgently desired for stabilizing LMB.

Therefore, we proposed a novel methodology to conquer the mentioned issues associated with insoluble $LiNO_3$ and inactive Li by utilizing the anion-exchange capability of functional I^--MgAl LDH. The interlayer channel of LDH exerts a dual effect, whereby it not only severs as $LiNO_3$ solubilizer to introduce NO_3^-, but also synchronously introduces I_3^-/I^- redox couple to rejuvenate inactive lithium. Concretely, $LiNO_3$ and calcined I^--MgAl LDH are simultaneously introduced in carbonate electrolyte. The NO_3^- anions of $LiNO_3$ infiltrate the interlayered gallery of LDH to form NO_3^--MgAl LDH, achieving the dissolution of $LiNO_3$ while playing a crucial role of sustainable nitrogen release. The Li_3N-rich SEI can be therefore constructed on Li anode surface, which effectively optimizes ion diffusion energy and mechanical strength.[30, 31] In addition, the exchanged iodine anions of I_3^- can spontaneously react with the Li_2O of SEI to continuously generate soluble LiI and IO_3^- ($3Li_2O + 3I_3^- = 6Li^+ + IO_3^- + 8I^-$) and convert the metallic dead Li fragments into LiI ($2Li + I_3^- = 2Li^+ + 3I^-$). Subsequently, LiI, as a medium of active Li^+ and I^-, reacts with the de-lithiation cathodes to regenerate I_3^-. At the same time, Li^+ is re-embedded into cathode to realize the rejuvenation of inactive Li (e.g. $LiFePO_4$: $2Li^+ + 3I^- + 2FePO_4 = 2LiFePO_4 + I_3^-$).[32, 33] Consequently, the CE of the Li||Cu cell with the designed electrolyte reaches up to 97.5%, and the capacity of Li||$LiFePO_4$ (a loading of 12 mg cm^{-2}) maintains a retention of 85% after 300 cycles at 3 C rate. In addition, the full cell with limited Li anode (N/P = 2) and anode-free cell exhibit higher discharge capacity retention. The emergence of a new class of solubilizer for low-solubility salts and the artful introduction of functional anions (such as I^-) based on utilizing the structural stability of 2D LDH are intriguing. Such strategy is of crucial importance to design 2D layered nanomaterials applied in the advanced electrolyte modification in LMBs.

2. Results and discussions

To synchronously solubilize $LiNO_3$ and introduce iodine medium, the functionalization of LDH additive is the key prerequisite for design concept (**Figure 1**). The CO_3^{2-}-intercalated MgAl LDH, with a well-defined morphology and stable structure, was fabricated via a hydrothermal method. It serves as the ideal precursor for the subsequent preparation of the I^- intercalated MgAl LDH (denoted as I^--MgAl LDH).[34],[35, 36] The subsequent low-temperature calcined I^--MgAl LDH (C-

I-LDH) effectively removes interlayer water molecules, thereby minimizing their impact on LMB and simultaneously retaining interlayer iodine ions. To explore the role of C-I-LDH as electrolyte additive, C-I-LDH is incorporated into commercial carbonate electrolyte (1 M $LiPF_6$, EC : DMC : DEC = 1:1:1, 5% FEC, annotated as BE) with $LiNO_3$. Utilizing the advantages of two-dimensional layered structure and anion-exchange capability, the NO_3^- from $LiNO_3$ spontaneously migrates into the anion sites within LDH interlayer for temporary storage, while the exchanged iodine medium exists in the electrolyte as I_3^- and I^-. This commendable design accomplishes not only the dissolution of $LiNO_3$ by establishing a NO_3^- storage gallery, but also enables the sustainable recycling and reactivation of inactive Li through its spontaneous reaction with I_3^-/I^-.

Figure S1Ai displays the X-ray powder diffraction (XRD) pattern of the precursors, revealing basal spacings of 0.76 nm that align with those previously reported for typical CO_3^{2-}-MgAl LDHs. After anion exchange of the CO_3^{2-}-MgAl LDH, the I^--MgAl LDH is obtained under meticulously controlled iodized salt and reaction condition. New series of intense basal reflections of I^--MgAl LDH appear at lower angles, accompanied by an increased d value of 1.10 nm (**Figure S1Aii**). The form of I^--intercalated has been indicated by UV-visible spectroscopy (**Figure S2**), confirming the successful exchange of CO_3^{2-} by I^-. The calcination temperature of I^--MgAl LDH was selected as 200 °C to eliminate the impact of interlayer water molecules on LMB and simultaneously prevent the decomposition of interlayered I^-, which was determined based on TG analysis (**Figure S1B**).[37] The calcined C-I-LDH exhibits almost the same crystal structure (**Figure S1Aiii**). During the process of anion-exchange and calcination, the morphologies of LDH basically maintain. Specifically, the scanning electron microscopy (SEM) image depicts hexagonal platelets morphology of CO_3^{2-}-MgAl LDH with lateral size about 2 μm (**Figure S1C**). The as-prepared I^--MgAl LDH also exhibits regular hexagonal platelets morphology (**Figure S1D**). Elemental analysis (**Figure S3A**) reveals an atomic ratio of Mg/Al/I at approximately 1.9/1.1/1, as well as the SEM mapping (**Figure S3B**) exhibits a homogeneous distribution of Mg, Al, O, and I chemical elements, indicating the successful exchange of I^- into the LDH interlayer. The EDS of C-I-LDH indicate only minimal iodine loss after calcination, essentially preserving the integrity of both structure and morphology (**Figure S4**).

To explore the working principle of C-I-LDH in electrolyte, C-I-LDH is added to BE electrolyte with and without $LiNO_3$, denoted as C-I-BE-LN and C-I-BE, respectively. The optical images in **Figure 2A** illustrate a significant difference in color for both electrolytes. C-I-BE-LN displays a distinct bright yellow color in the presence of $LiNO_3$, whereas C-I-BE remains initially milky white in the absence of $LiNO_3$. C-I-BE-LN and C-I-BE were filtered and washed by DMC to obtain the corresponding separated solid powders and solutions. The characteristic peaks of I^- and I_3^- can be simultaneously observed by UV-visible spectroscopy (**Figure 2Aiv**) of separated solution of C-I-BE-LN (**Figure 2Aiii**) as well as a bright yellow color,[38] indicating the presence of I^-/I_3^- couple after anion exchange. However, iodine in C-I-BE still intercalates in MgAl LDH in the form of I^- due to the lack of $LiNO_3$, thus displaying the original milky white color (**Figure 2Av**).

To investigate the microstructure and morphology of the C-I-BE-LN and C-I-BE powders in depth, XRD and SEM are performed. As shown in Figure **2B**, the interlayer spacing of C-I-BE remains unchanged, but interestingly, the interlayer spacing of C-I-BE-LN has shrunk to 0.97 nm.

The alteration in XRD of C-I-BE-LN substantiates the release of original I^- from the interlayer anion sites within LDH, subsequently replaced by NO_3^- from $LiNO_3$. The morphologies of C-I-BE-LN and C-I-BE basically unchanged with hexagonal plates, as displayed in **Figure 2C** and **Figure S5**. Notably, the elemental distribution of C-I-BE-LN (**Figure S6**) demonstrates that the atomic content of I decreases to 0.5%, while the content of N increases to 2.6%. Furthermore, the analysis of the changes in I and N content is conducted by inductively coupled plasma (ICP) and organic elemental analysis (EA) tests. As shown in **Table S1** and **S2**, a notable decline in I content is presented from the initial 36.0% in I^--MgAl LDH to 1.2% in C-I-BE-LN powders, while the N content of C-I-BE-LN powders (a value of 3.6%) is nearly identical to that of the pure NO_3^--MgAl LDH (4.32%), sufficiently proving that the successful anion exchange of NO_3^- by I^- within C-I-BE-LN.

X-ray photoelectron spectroscopy (XPS) is applied to intuitively observe the valence states of I and N elements in I^--MgAl LDH, C-I-LDH, and C-I-BE-LN powders. The XPS survey (**Figure 2D**) displays that the I peak intensity of I^--MgAl LDH and C-I-LDH at the binding energy of 615-640 eV is intense; while the I peak of C-I-BE-LN is markedly weakened. The detailed changes as shown in I 3d spectra (**Figure 2E**), which fully indicates that low-temperature calcination does not remove I, but I^- will be extract out the MgAl LDH interlayer due to anion exchange by NO_3^- of $LiNO_3$ in electrolyte. In addition, the N peak of I^--MgAl LDH and C-I-LDH at survey spectrum disappears due to absence of nitrogen source, while the N peak intensity of C-I-BE-LN can be clearly observed in the form of NO_3^- (**Figure 2F**). The N changes of C-I-BE-LN strongly confirm that the NO_3^- of $LiNO_3$ has been successfully inserted into interlayer anion sites of LDH in electrolyte to form NO_3^--MgAl LDH, achieving the solubilization of $LiNO_3$.

To gain in-depth insights into the anion exchange behavior of NO_3^- and I^- in electrolytes, density functional theory (DFT) is utilized to calculate the energy of MgAl LDH with varying anion intercalation. Two potential pathways are possible for the anion exchange process, which are illustrated in **Figure 2G**. Pathway 1 is characterized by the preferentially direct extrusion of I^- from the interlayer of I^--MgAl LDH, which forms an anionic vacancy prior to the insertion of NO_3^-. The alternative pathway initiates with the insertion of NO_3^- into the interlayer of I^--MgAl LDH, leading to the transient co-existence of I^- and NO_3^- in the interlayer, which subsequently extrudes the corresponding I^-. DFT calculations indicate that the initial step of the pathway 1 is nonspontaneous ($\Delta E > 0$). This suggests that it is challenging for the I^--MgAl LDH to spontaneously expel I^- to form vacancies that would allow the embedding of NO_3^-. The anion exchange behavior is more inclined to proceed through the second pathway, where NO_3^- spontaneously inserts into the interlayer of I^--MgAl LDH ($E < 0$), establishing a temporary coexistence with I^- in the interlayer and expelling I^- in the subsequent anion exchange process ($E < 0$).

The UV-visible spectra and XRD patterns are applied to validate the intrinsic mechanism and reversibility of the I_3^-/I^- redox couple upon reaction with cycled Li. The UV spectra of C-I-BE-LN exhibit the absorption peak of I^- (around 220 nm) and I_3^- (around 294 and 363 nm), attributing to iodine exchanged from the interlayer of MgAl LDH (**Figure 3A**). Cycled Li anode, derived from Li||Li symmetric cell with BE electrolyte for 12 cycles, was soaked into C-I-BE-LN electrolyte for reaction. The corresponding UV spectra verify the broadening absorption peak of I^- and weakening of I_3^-. Post-reaction with C-I-BE-LN electrolyte, the accumulations of primary SEI and Li dendrite with a blackened surface on cycled Li were obviously eliminated (**Figure S7**). Furthermore, the fading of solution color from the original yellow (**Figure S8**) is auxiliary evidence for I_3^- reduction. After soaked cycled Li in C-I-BE-LN, the characteristic peaks of Li significantly increased with enhanced crystallinity and reduced impurity peaks (**Figure 3B**), verifying the reduction of by-products such as Li_2O and dead Li. After the previous step, white $FePO_4$ was continuously added into electrolyte. The broad absorption of I^- in UV spectra disappeared, while the peaks of I_3^- recovered, indicating the regeneration of I_3^- during this process. The corresponding XRD pattern (**Figure 3C**) confirms the emergence of $LiFePO_4$ after the spontaneous lithiation of $FePO_4$, accompanied by the transformation of $LiFePO_4$ into light gray color (**Figure S9**).

To further investigate the spontaneity of I_3^-/I^- redox couple in recovering inactive Li, the reaction energies of I_3^-/I^- with various SEI chemical components and cathodes were calculated by DFT, as shown in **Figure 3D** and **4E**. I_3^- undergoes spontaneous reactions with Li_2O and dead Li with the $\Delta E < 0$. However, the reactions involving I_3^- and other SEI components, such as Li_3N, LiOH, LiF, Li_2CO_3, are non-spontaneous ($\Delta E > 0$, **Figure S10**). It indicates that I_3^- selectively eliminates undesirable components, while retaining effective SEI components such as Li_3N. In addition, the I_3^-/I^- redox couple energetically and spontaneously recovered irreversible Li capacity due to inserted inactive Li into the de-lithiated cathodes with an exothermic reaction of $\Delta E = -5.35$ eV. This demonstrates that the regeneration of I_3^-/I^- redox couple to rejuvenate inactive Li is a sustainable process.

The mentioned data and phenomena evidently suggest that the introduction of C-I-LDH into carbonate electrolyte achieves $LiNO_3$ solubilization through anion exchange. The interlayer of

LDH plays a pivotal role as NO_3^- buffer storage, as shown in **Figure 3D**. The exchanged I_3^- spontaneously reacts with metallic dead Li, facilitating the removal of Li debris. Meanwhile, I_3^- attacks the Li_2O in damaged SEI. Consequently, the I_3^-/I^- couple destructs the inactive Li on Li metal surface, exposing the fresh Li metal surface that is rapidly reduced and passivated by NO_3^- to construct a new and healthy NO_3^--derived SEI. LiI, as the primary reaction product of I_3^- with SEI and dead Li, re-embeds Li^+ source into cathode and reacts with de-lithiated $LiFePO_4$ during the charge process to regenerate I_3^-. This breakthrough in the recyclable recovery pathway of inactive Li based on I_3^-/I^- couple, not only realizes the reactivation and utilization of inactive Li, but also optimizes SEI film by the sustained release of NO_3^-.

The Li||Cu cells with BE, C-I-BE and C-I-BE-LN were employed to evaluate the Li^+ plating/stripping behavior. The cells with BE and C-I-BE experienced immediate short-circuiting, while the C-I-BE-LN cell maintained a higher average CE of 97.5% over 150 cycles (**Figure 4A**). The voltage-capacity profiles of C-I-BE-LN displayed the lower nucleation overpotential, which was attributed to the incorporation of $LiNO_3$ and C-I-LDH to construct NO_3^--derived SEI with high ionic conductivity, effectively regulating the Li^+ plating/stripping behavior. The Long-term cycling of Li||Li cells with different electrolytes was conducted at 0.5 mA cm^{-2} with 1 mAh cm^{-2}, as depicted in **Figure 4B**. The BE cell exhibited a huge upward overpotential trend, the C-I-BE cell maintained a relative overpotential of 20 mV until short-circuiting happened after 150 h (**Figure S11**), while the C-I-BE-LN cell delivered a lower overpotential of 15 mV and steady Li^+ plating/stripping performance over 600 h (**Figure S12**). The synergistic effect of $LiNO_3$ and C-I-LDH additives demonstrated advantageous outcomes for improving Li metal performance, as evidenced by lower overpotential and the absence of fluctuations in Li||Li cells under a series of current densities and areal capacities (**Figure 4C**).

Cyclic voltammetry (CV) tests were employed to assess the electrochemical stability of electrolytes. **Figure S13** presents the CV curves of Li||Cu cells with BE, C-I-BE, and C-I-BE-LN electrolytes, respectively. In contrast to BE and C-I-BE, an additional reduction peak around 1.6V appears in C-I-BE-LN, attributed to the decomposition of NO_3^-. No other reduction peaks associated with iodine decomposition are observed, owing to the spontaneous and recyclable reaction of I_3^- with Li_2O and dead Li. To further explore Li^+ plating/stripping kinetics, the CV curves of Li||Cu cells scanning from 2.5 to -0.2 V at 1 mV s^{-1} were tested (**Figure 4D**). Two predominant redox peaks near 0 V are attributed to Li^+ plating and stripping processes, respectively. Due to the presences of I_3^-/I^- couple and NO_3^-, the C-I-BE-LN cell displays the higher peak current density and lower Li deposition onset potential compared to C-I-BE and BE. This suggests that the C-I-BE-LN possesses the rapid Li^+ plating/stripping kinetics and great reversibility. The fast Li^+ transfer kinetics at interface of the C-I-BE-LN cell also reflects in the higher exchange current density (i_0) in Tafel plot (**Figure S14**) and smaller charge transfer resistance in EIS (**Figure 4E**).

Li^+ conductivity was calculated via the EIS obtained in stainless-steel||stainless-steel cells with different electrolytes (**Figure S15**). The C-I-BE-LN cell yields a substantially higher conductivity of 3.8 mS cm^{-1} than BE (3.5 mS cm^{-1}) and C-I-BE (2.8 mS cm^{-1}) at ambient temperature, as displayed in **Figure 4F**. Moreover, the effective Li^+ conductivity delivers an analogous trend of C-I-BE-LN (2.7 mS cm^{-1}) higher than BE (1.3 mS cm^{-1}) and C-I-BE (1.5 mS cm^{-1}). The trends clearly confirm that the introduction of $LiNO_3$ and C-I-LDH selectively exchanged and fixed anions (such as NO_3^-), facilitating the effective translocation of Li^+. After calculating by temperature-dependent ionic conductivity (the dots) and fitting based on the Arrhenius equation (**Figure S16**), the activation energy for diffusing through the bulk electrolyte of C-I-BE-LN (0.63 eV) is lower than C-I-BE (0.69 eV) and BE (0.73 eV) electrolyte, indicating that the designed C-I-BE-LN electrolyte facilitates transport of Li^+. Furthermore, the Li^+ transference number (t_{Li}^+) is commonly evaluated the mobility of Li^+ in the bulky electrolytes, calculated with the classical Vincent–Bruce method by measured in Li||Li cells. The corresponding potentiostatic polarization and EIS results are presented in **Figure S17-19**. The t_{Li}^+ for BE is 0.38, which is dramatically improved to 0.54 and 0.71 for C-I-BE and C-I-BE-LN, respectively. Combined with the synergistic effect of NO_3^- and I_3^-/I^- couple, the temporary storage of NO_3^- at LDH anion sites alleviates the participation of NO_3^- in Li^+ solvent sheath and decreases the binding energy as previously reported, which is conducive to fast migration of Li^+ in electrolyte.

To further investigate the energy barrier of Li^+ desolvating at SEI/electrolyte boundary (E_{act}) and Li^+ crossing through SEI film (E_{aint}), the temperature-dependent EIS tests were conducted on Li||Li cells, as shown in **Figure S20-22**. The activation energy of E_{act} and E_{aint} were obtained by fitting with Arrhenius equation based on EIS. Both E_{act} and E_{aint} of C-I-BE-LN are smaller than C-I-BE and BE, as displayed in **Figure 4G** and **Figure 4H**. In comparison to BE, the E_{act} of C-I-BE-LN (29.09 kJ mol^{-1}) significantly reduced about 28%, while E_{aint} (30.59 kJ mol^{-1}) also dramatically decreased about 33%. The diminished E_{act} indicates that the introduction of NO_3^- changes the coordination environment between Li^+ and solvents/anions. The absent participation of NO_3^- in Li^+ solvent sheath leads to the lower Li^+ solvent binding energy and Li^+ desolvation energy. When

Li^+ diffuses in the SEI films, the decreased E_{aint} demonstrates that the SEI generated by the sustained release of NO_3^- from LDH actively promotes the rapid transfer kinetics of Li^+ within SEI.

The etching XPS sputtered by Ar-ion on the cycled Li metal anode is conducted to confirm the in-depth chemical components of SEI film, as shown in the **Figure 5A-5C**. The decomposition products of electrolyte, LiF (684.4 eV) and Li_xPF_y (686.3 eV), are detected in F 1s spectra of all cells, exhibiting a distinct enhanced in intensity for LiF and a decrease for Li_xPF_y with increasing sputtering depth. Additionally, the cell with C-I-BE electrolyte displays the distinctive C-F (687.8 eV) within the F 1s spectrum, accompanied by a notable signal for metastable organics of C-O derived from the decomposition of carbonate solvents within the O 1s spectrum, indicating that the independent introduction of C-I-LDH may exacerbate the decomposition of the electrolyte. The N 1s spectra reveal the absence of a distinct N 1s peak in BE and C-I-BE due to the lack of N source. Conversely, C-I-BE-LN exhibits evident peaks of Li_3N at 398.9 eV, indicating the role of LDH as sustainable N source for the formation of Li_3N-massive SEI with ultrahigh Li ion conductivity.[39-41] Notably, the I signal is exclusively presented in C-I-BE at 618.4 eV and 629.9 eV, forming LiI as the SEI component. In stark contrast, the extraordinarily weak I 3d peaks in C-I-BE-LN strongly indicate that I_3^-/I^- in the co-exist of NO_3^- does not regulate SEI components as LiI. Therefore, the interlayered I^- of I^--MgAl LDH mainly plays the function of generating LiI to modified SEI, while the main mission of the I_3^-/I^- redox couple obtained by the anion exchange of LDH is to focus on removing Li_2O in SEI and dead Li dendrites, as reflected by the absence of Li_2O peaks in O1s spectra of C-I-BE-LN. In-depth XPS etching demonstrates that organic-rich SEI and irrepressible decomposition of solvent are easily generated in conventional carbonate-based electrolytes without additives. The presence of only I^- may also exacerbate the decomposition of the electrolyte, but the mechanism of I_3^-/I^- redox couple is markedly distinct with the simultaneous introduction of NO_3^-. The NO_3^- serves to passivate the surface of Li metal anode to inhibit the side reactions between the electrolyte and Li metal, while the I_3^-/I^- redox couple effectively facilitates the recovery of inactive Li. The more intuitive effect of this strategy is reflected in the morphologies of Li deposited on Cu collector with different electrolytes, as shown in **Figure 5D-5F** and **Figure S23**. Massive tree-like dendritic Li deposits in BE electrolyte, while Li tends to deposit a compact bulk structure in C-I-BE-LN. This implies that the nucleation and growth of Li metal can be readily regulated by the chemical composition of SEI. The obvious variation in XPS and Li deposition morphologies verify that the introduction of NO_3^- and I_3^-/I^- redox couple constitute effective strategy to solve the accumulation of inactive Li by fundamentally regulating SEI chemical components and avoiding dendritic Li.

The finite element analysis based on the surface film resistance method was performed by using COMSOL Multiphysics 5.6. Considering the above-mentioned characteristic component and morphology of SEI films, the corresponding model geometry and physical boundary nodes matching with different electrolytes were constructed in the physical field simulations to illustrate Li deposition behavior in different electrolytes (**Figure S24**). In BE electrolyte, Li^+ accumulates in some high ion conductivity areas (as hot spot), where the Li^+ flux follows streamlines, resulting in uneven Li nucleation and dendritic growth (**Figure 5G**). This phenomenon arises from the diversity and heterogeneity of SEI components due to the reaction of electrolyte with Li metal in BE. In addition, the impact of electrically isolated dead Li on deposition behavior also requires special consideration. As illustrated in **Figure 5H**, dead Li, constructed as a physical block, will distort and disrupt the Li^+ flux, ultimately leading to the growth of Li dendrite. For the C-I-BE electrolyte (**Figure 5I**), the SEI components, containing LiI due to the introduction of calcined I^--MgAl LDH, significantly influence Li growth. The simulation of C-I-BE electrolyte demonstrates that Li grows substantially higher to form bulk-like morphology deposition in the LiI region, compared to the poor ion-conductivity regions comprising Li_2O/LiF/Li_2CO_3. For the C-I-BE-LN electrolyte, the simultaneous introduction of calcined I^--MgAl LDH and $LiNO_3$ effectively alleviates electrolyte decomposition, reducing the LiF component in SEI. Moreover, the I_3^-/I^- redox couple plays a crucial role in scavenging the poor ion conductors of Li_2O and dead Li, while the $LiNO_3$ contributes to form the Li_3N-rich SEI with high ion-conductivity. The synergistic effects of the mentioned roles lead to a more uniform Li^+ flux and concentration gradient distribution, forming a planar and dense Li deposition in C-I-BE-LN electrolyte (**Figure 5J**), which is well consistent with the SEM characterization of SEI.

The electrochemical effect and feasibility of the synergistic I_3^-/I^- and NO_3^- are evaluated in full cells. Before assembling full cells, the electrochemical oxidation window of proposed electrolytes is evaluated by linear sweep voltammetry (LSV) in Li||stainless-steel cell (**Figure S25**). The electrochemical stability voltages of C-I-BE-LN (≈4.4 V) are not obviously declined except for an electrochemical oxidation reaction of I^- to I_3^- at 3.6 V.[42] In contrast, the oxidation stability of C-I-BE is greatly destroyed, narrowing the oxidation window to ~3.7 V, resulting in the failure of full cells when operating in a broader window, as depicted in **Figure S26**. The impressive electrochemical performance of Li||$LiFePO_4$ full cells with C-I-BE-LN is embodied in significantly enhanced reversibility and prolong lifespan, with the higher discharge capacity retention of 85% after 300 cycles at 3 C rate (**Figure 6A, Figure S27**). Similar trends in rate capacity also are obtained due to the lower interface resistance (**Figure S28**), as shown in **Figure 6B**, **Figure S29** and summarized in **Table S3**. The high-energy Li||NCM523 ($LiNi_{0.5}Co_{0.2}Mn_{0.3}O_2$) full cell with C-I-BE-LN electrolyte also exhibits superior cycling stability with capacity retention of 91% after 110 cycles, while the BE experiences rapid fading (**Figure 6C**). Above results tentatively confirm the practicalities of simultaneously introducing NO_3^- and I_3^-/I^- to achieve stable Li anode interface and recover irreversible inactive Li capacity.

The excellent performance of full cells with C-I-BE-LN electrolyte motivates us to conduct evaluations in Li@Cu||$LiFePO_4$ cells (a limited Li capacity of 2.0 mAh cm^{-2}, N/P = 2) and Cu||$LiFePO_4$ cells (anode-free). These evaluations avoid the exaggeration of LMB performances caused by extremely excessive Li sources, allowing for a more practical assessment and exploration of the underlying mechanisms of capacity loss. Clearly, the Li@Cu||$LiFePO_4$ (**Figure 6D**) and Cu||$LiFePO_4$ (**Figure 6E**) cells with C-I-BE-LN electrolyte deliver prime cyclability than BE, indicating that the C-I-BE-LN electrolyte benefits the maintenance of available Li^+ and sustainable operation in a practical cell setting. Specifically, the cells with BE electrolyte exhibit a markedly inferior Coulombic efficiency compared to the C-I-BE-LN, leading to significantly lower initial capacity and a pronounced capacity decay under long-term cycling. The results indicate that the simultaneous incorporation of I_3^-/I^- and NO_3^- into the C-I-BL-N electrolyte, along with the optimization of the SEI and the rejuvenating of inactive Li, markedly enhances both the Coulombic efficiency and the reversible capacity of the batteries. To further demonstrate the recovery effect of

I_3^-/I^- on inactive Li, the Li cycled 200 times is assembled with de-lithiated $LiFePO_4$ to conduct a long-term cycle at 1 C, as shown in **Figure 6F**, **6G** and **6H**. In contrast to BE, operating for only 10 cycles with a significant capacity fluctuates, C-I-BE-LN maintains a stable lifespan over 90 cycles with an initial capacity of 150.7 mAh g^{-1}. This strongly supports the role of I_3^-/I^- on rejuvenating inactive Li in ways of restoring Li^+ in cathode and achieving reversible capacity. To exclude the effect of self-discharge phenomenon caused by introducing I_3^-/I^-, the discharge capacity of full charged Li||$LiFePO_4$ cells after standing for 0 h, 12 h, 24 h and 48 h is tested, as displayed in **Figure 6I** and **Figure S30**. After standing 48 h, the discharge capacity of BE decays from 149.2 to 132.1 mAh g^{-1} (17.1 mAh g^{-1} loss), whereas only a capacity loss of 1 mAh g^{-1} in C-I-BE-LN is essentially negligible. Above results indicate that the Li metal surface is passivated by NO_3^- due to the coexistence of calcined I^--MgAl LDH and $LiNO_3$, which allows for the quick construction of improved SEI with electronic insulation and high ion-conductivity, thus effectively restraining the self-discharge state.

3. Conclusion

In this work, the two-dimensional calcined I^--MgAl LDH has been designated to store and release NO_3^- and I^- in carbonate electrolyte via its capability of anion exchange. Consequently, the solubility of $LiNO_3$ can be greatly promoted and inactive Li can be recovered. Combining with experiments and theoretical analysis, LDH plays a crucial role through storage and sustainable release of NO_3^- in constructing Li_3N-rich SEI to suppress the growth of Li dendrites. The I_3^-/I^- redox couple extracted by anion exchange is indispensable for rejuvenating inactive Li from the already formed Li dendrites and derived dead Li. The proposed electrolyte additive strategy with C-I-LDH and $LiNO_3$ significantly improves Li^+ transfer kinetics and optimizes the morphology of Li deposition, as reflected by remarkable enhancement of Li^+ stripping/plating CE up to 97.5% in Li||Cu cells, superior cycling of Li||$LiFePO_4$ with 85% retention after 300 cycles at 3 C, and 91% retention after 110 cycles at 0.5 C for Li||NCM523 full cells. The current strategy inspires the electrolyte engineering via storage and sustainable release of effective additives, and therefore presents promising potential for the development of high-energy LMB.

Declaration of Competing Interest

The authors declare no competing financial interests.

ACKOWLEDGEMENTS

F.W. and Z.Z. contributed equally to this work. The authors acknowledge the financial support by National Natural Science Foundation of China (U20A20123, 22379166, 51874357), Natural Science Foundation for Distinguished Young Scholars of Hunan Province (2022JJ10089) and Central South University Innovation-Driven Research Programme (2023CXQD034). G. C. acknowledges the support from the 100 Talented program of Hunan Province. This work was supported in part by the High Performance Computing Center of Central South University.

Appendix A. Supporting information.

Supplementary data associated with this article can be found in the online version.

References

[1] Li T, Zhang X-Q, Shi P, et al. Fluorinated solid-electrolyte interphase in high-voltage lithium metal batteries. Joule 2019; 3: 2647-2661

[2] Qing P, Huang S, Naren T, et al. Interpenetrating LiB/Li_3BN_2 phases enabling stable composite lithium metal anode. Sci Bull 2024; 69: 2842-2852

[3] Li Z, Yao YX, Zheng M, et al. Electrolyte design enables rechargeable $LiFePO_4$/graphite batteries from −80 °c to 80 °c. Angew Chem Int Ed Engl 2024; e202409409.

[4] Qin Z, Zhang Y, Luo W, et al. A universal molten salt method for direct upcycling of spent ni-rich cathode towards single-crystalline li-rich cathode. Angew Chem Int Ed Engl 2023; 62: e202218672

[5] Chen J, Cheng Z, Liao Y, et al. Selection of redox mediators for reactivating dead li in lithium metal batteries. Adv Energy Mater 2022; 12: 2201800

[6] Li Y, Wang T, Chen J, et al. An artificial interfacial layer with biomimetic ionic channels towards highly stable li metal anodes. Sci Bull 2023; 68: 1379-1388

[7] Lin L, Qin K, Hu YS, et al. A better choice to achieve high volumetric energy density: Anode-free lithium-metal batteries. Adv Mater 2022; 34: e2110323

[8] Chen X-R, Yan C, Ding J-F, et al. New insights into “dead lithium” during stripping in lithium metal batteries. J Energy Chem 2021; 62: 289-294

[9] Liu H, Holoubek J, Zhou H, et al. An anode-free li metal cell with replenishable li designed for long cycle life. Energy Stor Mater 2021; 36: 251-256

[10] Zhong Y, Xie X, Zeng Z, et al. Triple-function hydrated eutectic electrolyte for enhanced aqueous zinc batteries. Angew Chem Int Ed Engl 2023; 135: e202310577

[11] Hu Z, Deng W, He B, et al. Self-adaptive 3d skeleton with charge dissipation capability for practical li metal pouch cells. Nano Energy 2022; 93: 106805

[12] Tan YH, Lu GX, Zheng JH, et al. Lithium fluoride in electrolyte for stable and safe lithium-metal batteries. Adv Mater 2021; 33: e2102134

[13] Fu J, Ji X, Chen J, et al. Lithium nitrate regulated sulfone electrolytes for lithium metal batteries. Angew Chem Int Ed 2020; 59: 22194-22201

[14] Zhuo Han DZ, Haixian Wang, Guorui Zheng, Ming Liu, Yanbing He. Research progress and prospect on electrolyte additives for interface reconstruction of long-life ni-rich lithium batteries. Acta Phys. -Chim. Sin. 2023; 2307034-

[15] Weng YT, Liu HW, Pei A, et al. An ultrathin ionomer interphase for high efficiency lithium anode in carbonate based electrolyte. Nat Commun 2019; 10: 5824

[16] Wang J, Li L, Hu H, et al. Toward dendrite-free metallic lithium anodes: From structural design to optimal electrochemical diffusion kinetics. ACS Nano 2022; 16: 17729-17760

[17] Liu F, Xu R, Wu Y, et al. Dynamic spatial progression of isolated lithium during battery operations. Nature 2021; 600: 659-663

[18] Lin D, Liu Y, Chen W, et al. Conformal lithium fluoride protection layer on three-dimensional lithium by nonhazardous gaseous reagent freon. Nano Lett 2017; 17: 3731-3737

[19] Lin D, Liu Y, Liang Z, et al. Layered reduced graphene oxide with nanoscale interlayer gaps as a stable host for lithium metal anodes. Nat Nanotechnol 2016; 11: 626-632

[20] Gao Z, Zhang S, Huang Z, et al. Protection of li metal anode by surface-coating of pvdf thin film to enhance the cycling performance of li batteries. Chin Chem Lett 2019; 30: 525-528

[21] Jin CB, Zhang XQ, Sheng OW, et al. Reclaiming inactive lithium with a triiodide/iodide redox couple for practical lithium metal batteries. Angew Chem Int Ed Engl 2021; 60: 22990-22995

[22] Wen Z, Fang W, Chen L, et al. Anticorrosive copper current collector passivated by self-assembled porous membrane for highly stable lithium metal batteries. Adv Funct Mater 2021; 31:

[23] Li X, Zhao R, Fu Y, et al. Nitrate additives for lithium batteries: Mechanisms, applications, and prospects. eScience 2021; 1: 108-123

[24] Fang W, Wen Z, Chen L, et al. Constructing inorganic-rich solid electrolyte interphase via abundant anionic solvation sheath in commercial carbonate electrolytes. Nano Energy 2022; 104: 107881

[25] Zhang H, Yu Z, Cheng J, et al. Halide/sulfide composite solid-state electrolyte for li-anode based all-solid-state batteries. Chin Chem Lett 2023; 34: 108228

[26] Wang F, Wen Z, Zheng Z, et al. Memory effect of mgal layered double hydroxides promotes lino3 dissolution for stable lithium metal anode. Adv Energy Mater 2023; 13: 2203830

[27] Jin D, Roh Y, Jo T, et al. Robust cycling of ultrathin li metal enabled by nitrate-preplanted li powder composite. Adv Energy Mater 2021; 11: 2003769

[28] Liu Y, Lin D, Li Y, et al. solubility-mediated sustained release enabling nitrate additive in carbonate electrolytes for stable lithium metal anode. Nat Commun 2018; 9: 3656

[29] Zhang X-Q, Chen X, Hou L-P, et al. Regulating anions in the solvation sheath of lithium ions for stable lithium metal batteries. ACS Energy Lett 2019; 4: 411-416

[30] Yan C, Yao Y-X, Chen X, et al. lithium nitrate solvation chemistry in carbonate electrolyte sustains high-voltage lithium metal batteries. Angew Chem Int Ed Engl 2018; 130: 14251-14255

[31] Park K, Yu B-C, Goodenough JB. Li_3N as a cathode additive for high-energy-density lithium-ion batteries. Adv Energy Mater 2016; 6: 1502534

[32] Jin C, Liu T, Sheng O, et al. Rejuvenating dead lithium supply in lithium metal anodes by iodine redox. Nat Energy 2021; 6: 378-387

[33] Wen Z, Fang W, Wu X, et al. High-concentration additive and triiodide/iodide redox couple stabilize lithium metal anode and rejuvenate the inactive lithium in carbonate-based electrolyte. Adv Funct Mater 2022; 32: 2204768

[34] Sun P, Chen F, Zhou W, et al. Superionic conduction along ordered hydroxyl networks in molecular-thin nanosheets. Mater Horiz 2019; 6: 2087-2093

[35] Prasanna SV, Kamath PV, Shivakumara C. Interlayer structure of iodide intercalated layered double hydroxides (ldhs). J Colloid Interface Sci 2010; 344: 508-512

[36] Iglesias L, Walther C, Medina F, et al. A comprehensive study on iodine uptake by selected ldh phases via coprecipitation, anionic exchange and reconstruction. J Radioanal Nucl Ch 2015; 307: 111-121

[37] Dinh TD, Zhang D, Tuan VN. High iodine adsorption performances under off-gas conditions by bismuth-modified znal-ldh layered double hydroxide. RSC Adv 2020; 10: 14360-14367

[38] Ma R, Liang J, Takada K, et al. Topochemical synthesis of co-fe layered double hydroxides at varied fe/co ratios: Unique intercalation of triiodide and its profound effect. J Am Chem Soc 2011; 133: 613-620

[39] Piao N, Liu S, Zhang B, et al. Lithium metal batteries enabled by synergetic additives in commercial carbonate electrolytes. ACS Energy Lett 2021; 6: 1839-1848

[40] Yan C, Yao YX, Chen X, et al. Lithium nitrate solvation chemistry in carbonate electrolyte sustains high-voltage lithium metal batteries. Angew Chem Int Ed Engl 2018; 57: 14055-14059

[41] Fang W, Wen Z, Wang F, et al. Triple-function eutectic solvent additive for high performance lithium metal batteries. Sci Bull 2024; 69: 1686-1696

[42] Zhao Y, Wang L, Byon HR. High-performance rechargeable lithium-iodine batteries using triiodide/iodide redox couples in an aqueous cathode. Nat Commun 2013; 4: 1896

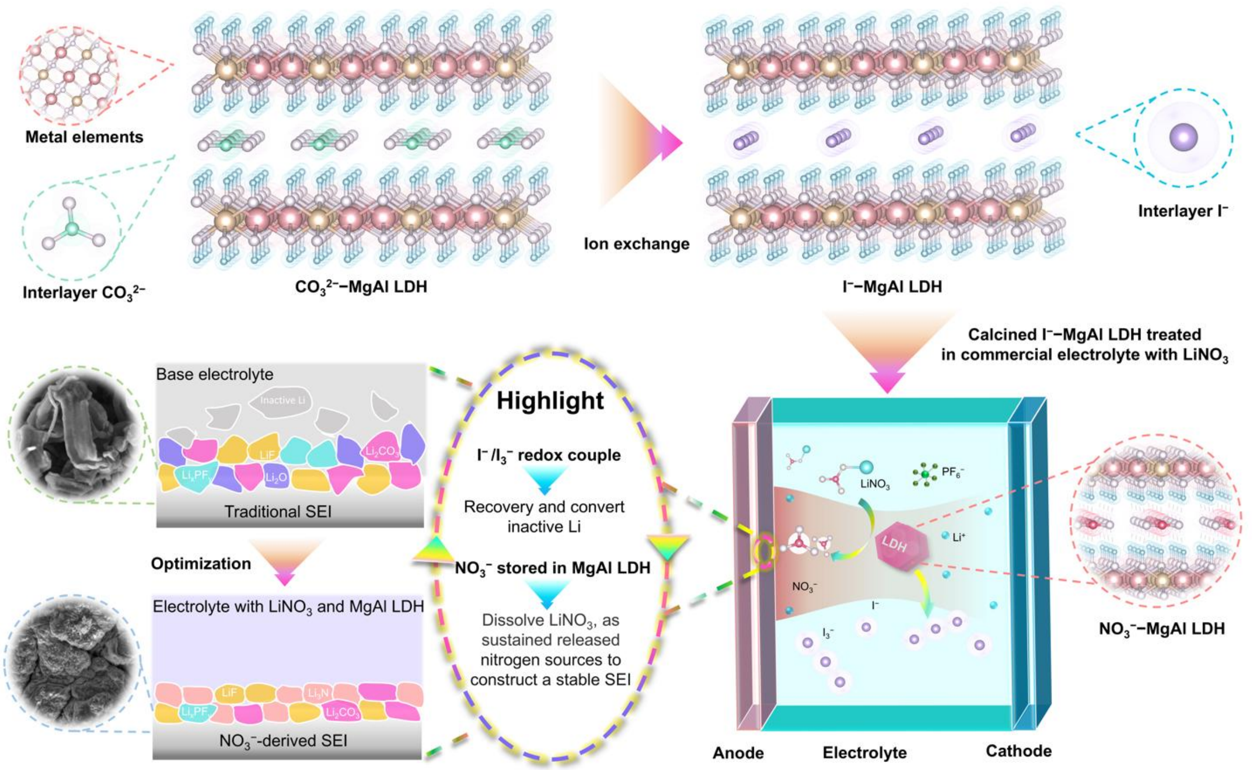

Figure 1. Schematic diagram of the MgAl LDH structure and electrolyte engineering design principle for LMB.

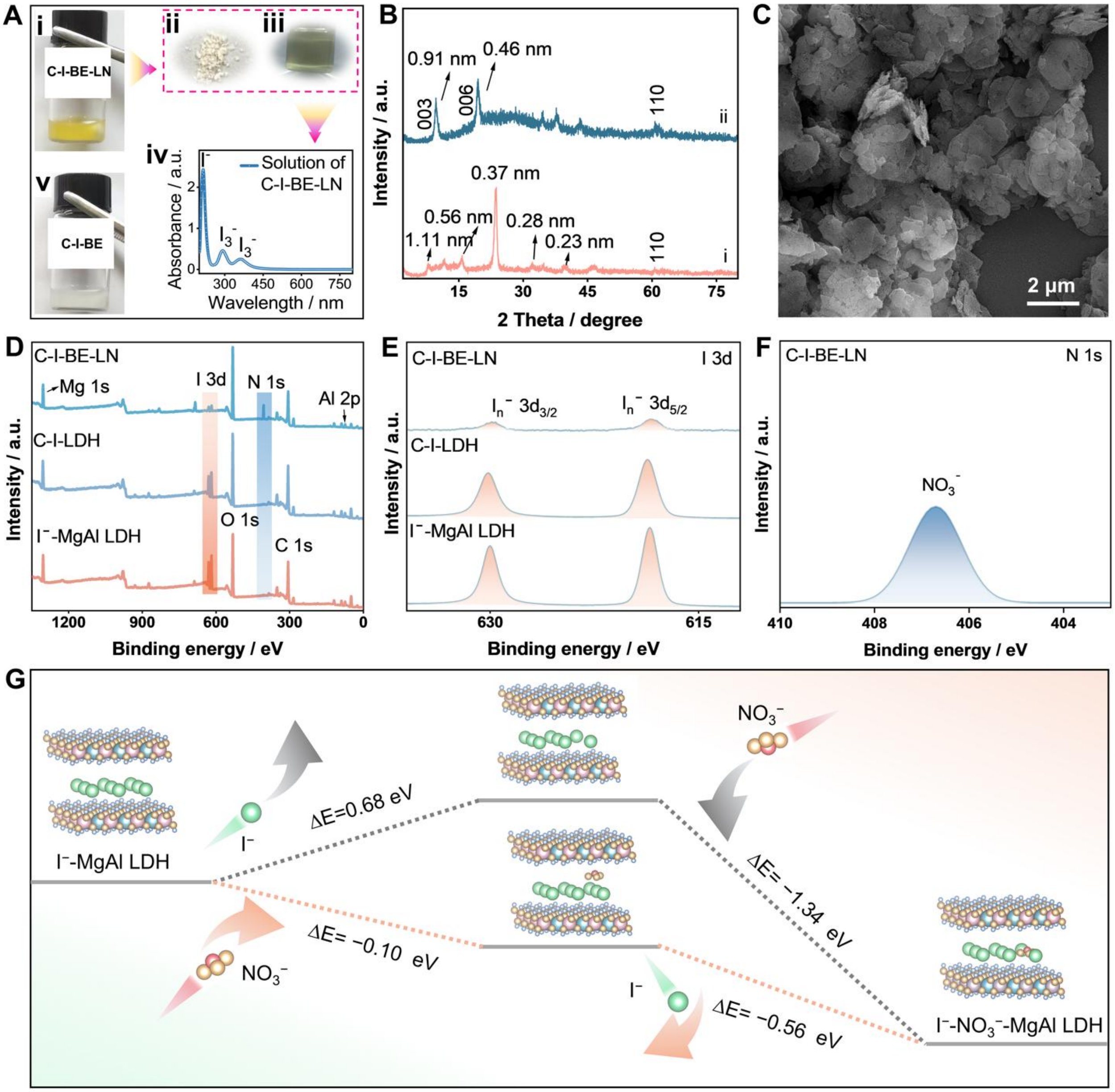

Figure 2. The engineering research of dissolving $LiNO_3$ via anion exchange I^- for NO_3^- in MgAl LDH. (A) Digital photos of i) C-I-BE-LN, ii) C-I-BE-LN solid powders after filtration and washed by DMC, iii) the separated solution of C-I-BE-LN after filtration, iv) the UV-visible spectroscopy of the separated solution of C-I-BE-LN, v) digital photos of C-I-BE. (B) XRD patterns of the i) C-I-BE, ii) C-I-BE-LN powders. (C) SEM image of C-I-BE-LN powders. (D) XPS survey spectrum, (E) I 3d spectra, and (F) N 1s spectra of the I^--MgAl LDH, C-I-LDH and C-I-BE-LN, (G) Two routes for I^--MgAl LDH anion exchange with NO_3^- in electrolyte predicted by DFT calculation.

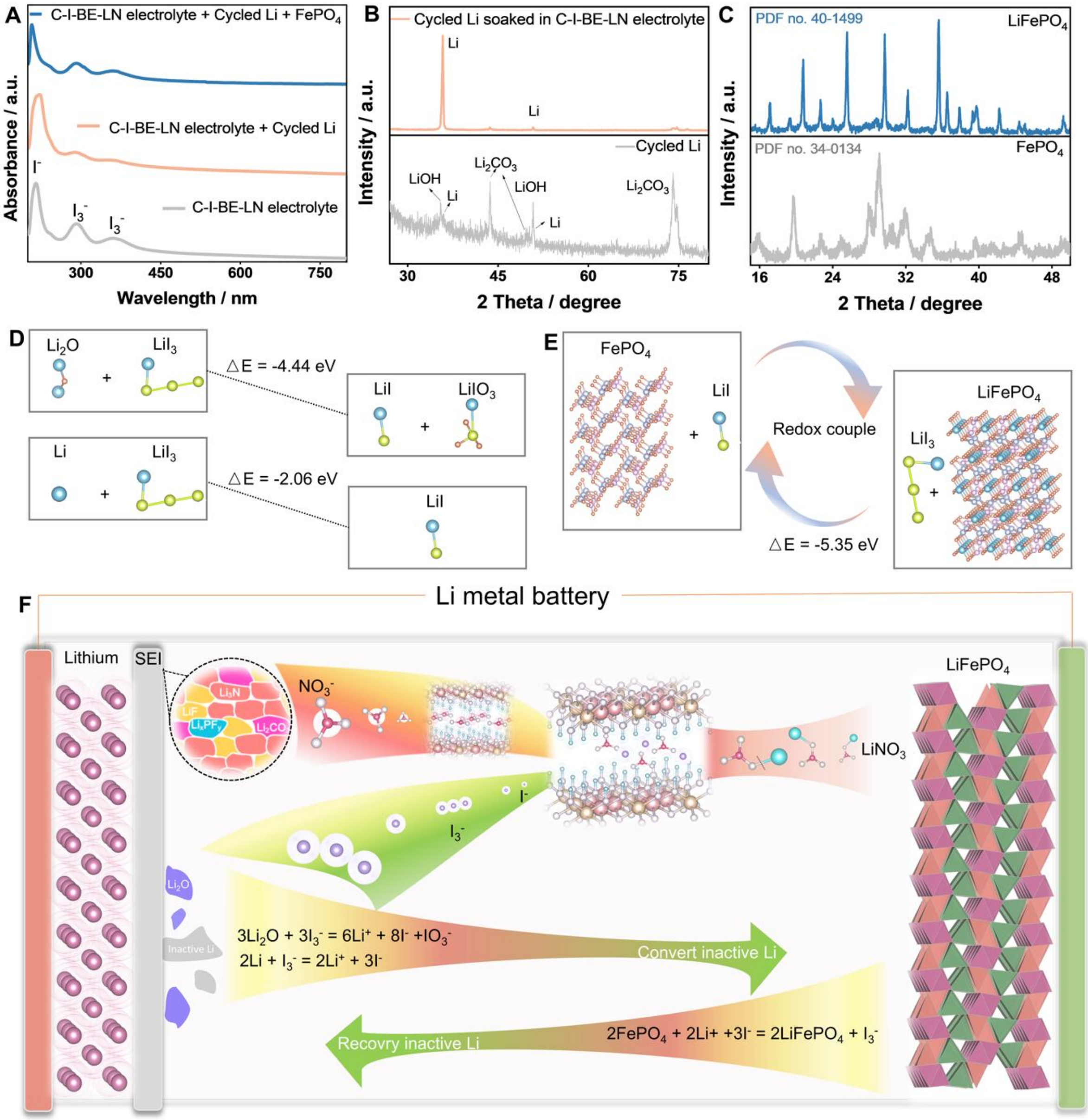

Figure 3. Mechanism for rejuvenating inactive Li. (A) UV-visible spectra of C-I-BE-LN electrolyte, the cycled Li soaked in C-I-BE-LN electrolyte, the $FePO_4$ soaked in cycled Li-reacted C-I-BE-LN electrolyte. (B) XRD patterns of cycled Li before and after soaked in C-I-BE-LN electrolyte. (C) XRD patterns of $FePO_4$ and lithiated $FePO_4$ soaked in the C-I-BE-LN electrolyte. (D) The reaction energy change (ΔE) of the exchanged I_3^- reacts with the Li_2O of SEI and metallic dead Li fragments. (E) Regeneration of inactive Li and reaction energy change (ΔE) with I_3^-/I^- redox couple. (F) Schematic illustration of adding I^--MgAl LDH to solubilize $LiNO_3$ and the sustainable reaction of reactivating inactive Li in carbonate electrolyte.

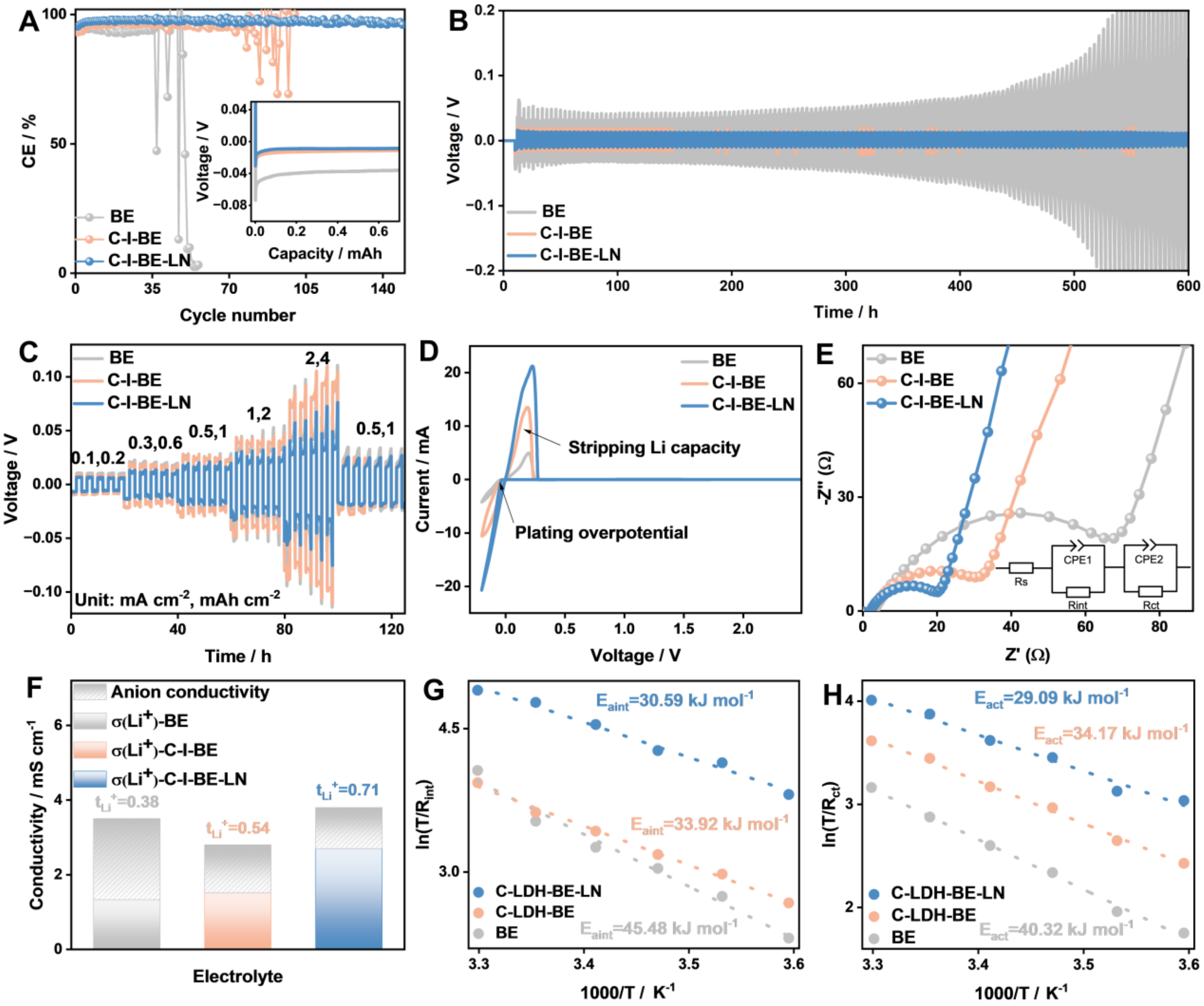

Figure 4. (A) CEs of Li||Cu asymmetric cells with different electrolytes at 0.5 mA cm^{-2} with capacity of 1.0 mAh cm^{-2}. Inserted Figure is voltage-capacity profiles of Li deposition on Cu foil at 0.5 mA cm^{-2}. (B) Galvanostatic cycling performance of Li||Li symmetric cells at 0.5 mA cm^{-2} with capacity of 1.0 mAh cm^{-2}. (C) The plating/stripping voltage profiles of Li||Li cells in a series of current densities and areal capacities. (D) Cyclic voltammetry curves of Li||Cu cells under a sweep rate of 1 mV s^{-1}. (E) Electrochemical impedance spectra (EIS) of cycled Li||Cu cells (after 12 cycles). (F) Comparisons of ionic conductivity and Li^{+} transference number. (G) and (H) The activation energies of R_{int} and R_{ct} derived from Nyquist plots.

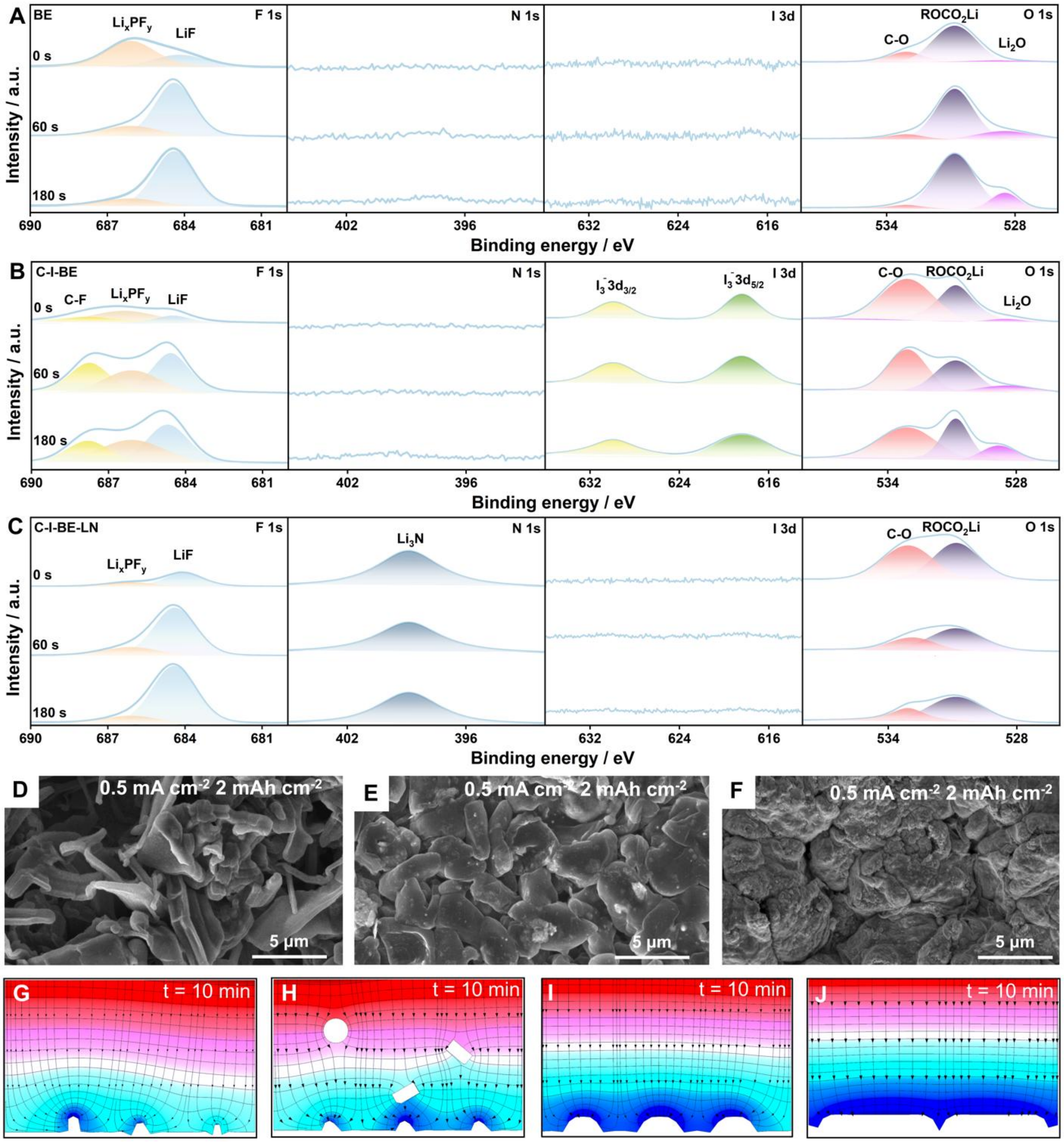

Figure 5. Characterizations of Li_3N Enhanced SEI. The in-depth XPS spectra of Li metal surface after 12 cycles of plating in Li||Li cells in (A) BE, (B) C-I-BE, (C) C-I-BE-LN electrolyte. SEM images of Li deposited morphologies with (D) BE, (E) C-I-BE, and (F) C-I-BE-LN electrolytes. The COMSOL simulation snapshots of Li deposition morphology for (G) BE, (H) dead Li^0 in SEI, (I) C-I-BE, (J) C-I-BE-LN.

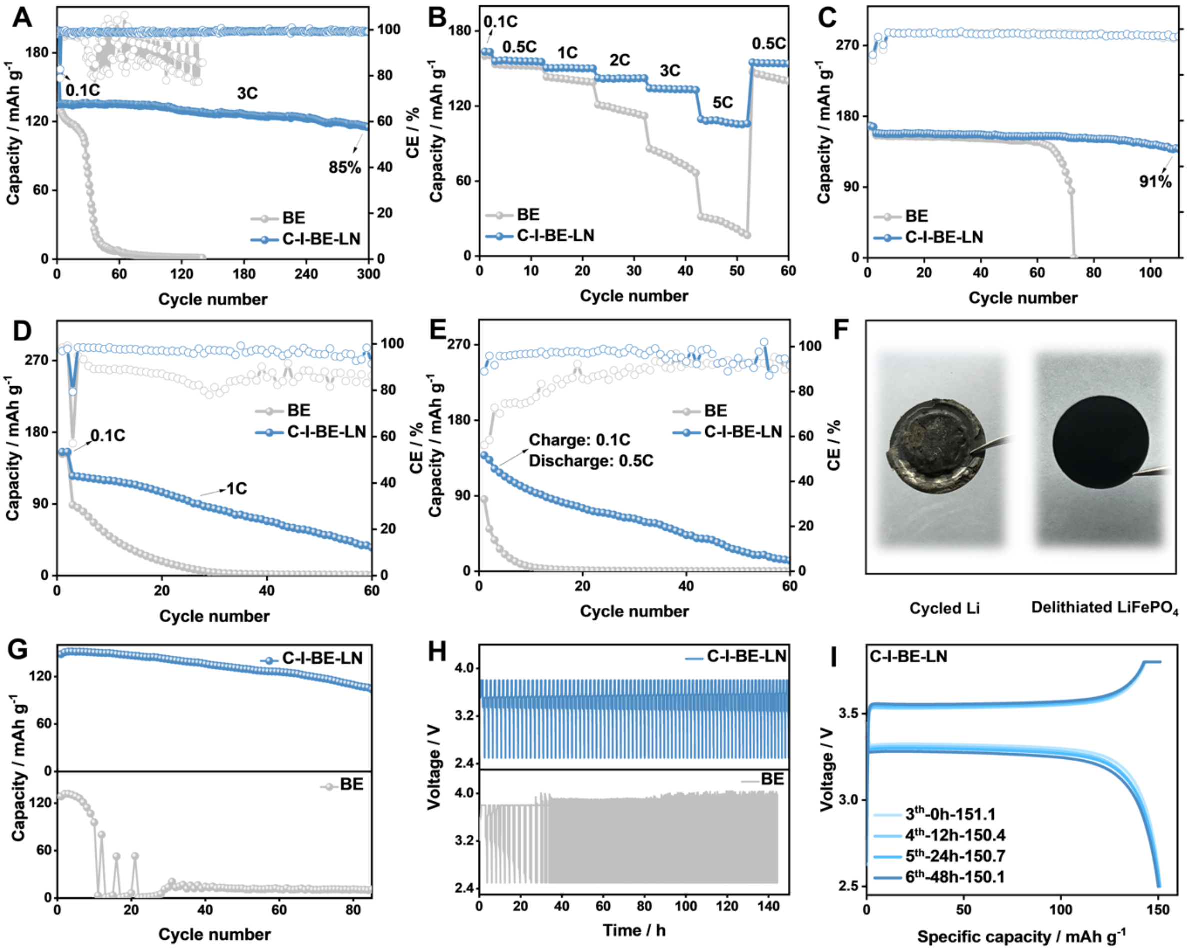

Figure 6. Electrochemical performance of the full cells. (A) Cycling performances of the Li||LiFePO$_4$ (loading of 12 mg cm^{-2}) cells with different electrolytes at 3 C. (B) Rate performance of Li|| LiFePO$_4$ cells at a step rate of 0.5 C to 5 C. (C) Cycling performances of the Li||NCM523 cells at 0.5 C. (D) Cycling performance of Li@Cu||LiFePO$_4$ with a limited Li capacity of 2.0 mAh cm^{-2} (N/P = 2). (E) Cycling performance of Cu||LiFePO$_4$ cells charged at 0.1 C and discharged at 0.5 C. (F) The digital photos of cycled Li and delithiated LiFePO$_4$. (G) The cycling performance in cycled Li||delithiated LiFePO$_4$ cells at 1 C. (H) The corresponding charge-discharge profiles in cycled Li||delithiated LiFePO$_4$ cells. (I) Discharge and charge curves of Li||LiFePO$_4$ cells after standing 12 h, 24 h and 48 h in C-I-BE-LN.